AGU PUBLICATIONS

JGR

Journal of Geophysical Research: Space Physics

RESEARCH ARTICLE
10.1002/2016JA023024

Key Points:
- The majority of EPBs in June solstice develop around midnight via RT instability due to uplift of equatorial *F* layer
- Formation of steep vertical density gradient (high KF) region at higher altitudes is the key factor for enhanced growth rate
- Weak westward electric field and equatorward wind set favorable conditions for development of EPBs around midnight hours of June solstice

Correspondence to:
K. K. Ajith,
ajithkk2007@gmail.com

Citation:
Ajith, K. K., S. Tulasi Ram, M. Yamamoto, Y. Otsuka, and K. Niranjan (2016), On the fresh development of equatorial plasma bubbles around the midnight hours of June solstice, *J. Geophys. Res. Space Physics*, *121*, doi:10.1002/2016JA023024.

Received 3 JUN 2016
Accepted 30 AUG 2016
Accepted article online 6 SEP 2016

On the fresh development of equatorial plasma bubbles around the midnight hours of June solstice

K. K. Ajith[1], S. Tulasi Ram[1], M. Yamamoto[2], Y. Otsuka[3], and K. Niranjan[4]

[1]Indian Institute of Geomagnetism, New Bombay, India, [2]Research Institute for Sustainable Humanosphere, Kyoto University, Kyoto, Japan, [3]Institute for Space-Earth Environment Research, Nagoya University, Nagoya, Japan, [4]Department of Physics, Andhra University, Visakhapatnam, India

Abstract Using the 47 MHz Equatorial Atmosphere Radar (EAR) at Kototabang, Indonesia, the nocturnal evolution of equatorial plasma bubbles (EPBs) was examined during the moderate solar activity years 2011–2012. While the evolution of EPBs was mostly (86%) confined to post sunset hours (1900–2100 LT) during equinoxes, in contrast, the majority of EPBs (~71%) in June solstice found evolve around the midnight hours (2200–0300 LT). The mechanisms behind the fresh evolution of summer time midnight EPBs were investigated, for the first time, through SAMI2 model simulations with a realistic input of background ExB drift variation derived from CINDI IVM on board C/NOFS satellite. The term-by-term analysis of linear growth rate of RT instability indicates that the formation of high flux tube electron content height gradient (K^F) (steep vertical gradient) region at higher altitudes is the key factor for the enhanced growth rate of RT instability. The responsible factors are discussed in light of relatively weak westward zonal electric field in the presence of equatorward neutral wind and bottomside recombination around the midnight hours of June solstice. The effects of neutral winds and weak westward electric fields on the uplift of equatorial *F* layer were examined separately using controlled SAMI2 simulations. The results indicate that relatively larger linear growth rate is more likely to occur around midnight during June solstice because of relatively weak westward electric field than other local times in the presence of equatorward meridional wind.

1. Introduction

The nighttime equatorial ionosphere is responsible for a number of electrodynamic processes often leading to the formation of equatorial plasma bubbles (EPBs). These irregularities are characterized by the depletions in the plasma, generated by spatial large scale density perturbations that serve as a seeding source for the development of EPBs [*Tsunoda et al*., 2011; *Tulasi Ram et al*., 2012, 2014]. Since the scintillations caused by EPBs result in outages of the communication and navigation systems, understanding the day-to-day variability of this phenomenon is very important. According to our present understanding, EPBs are developed at the bottomside *F* layer through Rayleigh-Taylor (RT) instability, preferably, during post sunset hours when the *F* layer is elevated to higher altitude due to the prereversal enhancement (PRE) in the zonal electric field [*Farely* et al., 1986]. Besides the height rise of the *F* layer, the vertical density gradient that antiparallel to gravity steepens at the bottomside *F* region due to the rapid recombination at regions below the *F* layer after sunset. These conditions make the post sunset period more conducive for the development of EPBs [*Kelley*, 1989; *Tulasi Ram et al*., 2006]. Beginning with the generation and growth phase, the bubble nonlinearly rises in to the topside ionosphere via polarization electric fields within them. Once developed, these EPBs generally drift eastward with velocities ranging from 50 to 200 m/s [*Aarons et al*., 1980; *Bhattacharyya et al*., 2001]. The seasonal and longitudinal variability of EPB occurrence is influenced by the alignment of sunset terminator with magnetic meridian. The EPB occurrence is higher for equatorial locations where the local magnetic field lines align with the sunset terminator. More specifically, in the Asian sector, the occurrence of EPBs is generally higher during the equinox months, where the declination angle of geomagnetic field line is nearly zero and less during the solstices [*Tsunoda*, 1985; *Tulasi Ram et al*., 2006]. However, in the South American sector where the magnetic declination is negative, the EPB occurrence enhances during December solstice months [*Abdu et al*., 1981].

However, a different class of EPB irregularities often observed around and after the midnight hours of the June solstice those having different characteristic features from post sunset EPBs. The occurrence of these summertime midnight irregularities was confirmed using various observational techniques like ionosondes [*Subbarao and Krishna Murthy*, 1994; *Sastri*, 1999], VHF scintillation [*Krishna Moorthy et al*., 1979;

Rama Rao et al., 2005], VHF backscatter radar [*Otsuka et al*., 2009; *Yokoyama et al*., 2011; *Nishioka et al*., 2012], and topside in situ observations from low Earth orbiting satellites [*Dao et al*., 2011; *Yizengaw et al*., 2013]. The occurrence of these midnight EPBs maximizes during the low solar activity periods, and their occurrence frequency can be even larger than that of post sunset EPBs of equinox during solar minimum [e.g., *Heelis et al*., 2010]. Using the ionosonde observations, *Subbarao and Krishna Murthy* [1994] reported that the post midnight irregularities manifest as frequency-type spread *F* on ionograms. *Otsuka et al*. [2009] studied the dynamics and occurrence of the field aligned irregularities (FAIs) at midnight hours during 2006 to 2007 using 30.8 MHz VHF radar at Kototabang, Indonesia, and reported that these midnight FAIs are weaker than the post sunset FAIs and were not accompanied with GPS scintillation. *Otsuka et al*. [2009] and *Ajith et al*. [2015] have shown that most of the EPBs around and after midnight hours do not exhibit significant zonal drift, whereas about 15% of them show clear westward drifts. Using the fan sector backscatter maps of Equatorial Atmosphere Radar (EAR), *Ajith et al*. [2015] found that majority of these EPBs are freshly evolving around midnight, however, exhibit slower vertical growth velocities than the post sunset EPBs [*Dao et al*., 2016].

From the extensive studies during past few decades, the generation mechanisms of post sunset EPBs were fairly well understood. However, the responsible mechanisms behind the formation of EPBs around and after midnight were not clearly known. Some attempts are made to understand the plausible background ionospheric conditions for the development of EPBs around midnight hours. Using Equatorial Atmosphere Radar (EAR), *Yokoyama et al*. [2011] have studied a few cases of post midnight EPBs over Kototabang. They have reported these post midnight EPBs as upwelling plumes and suggested RT instability could be the generation mechanism. From the simultaneous observations using radar and ionosonde over Indonesian sector, *Nishioka et al*. [2012] reported that the uplift of equatorial *F* layer enhances the gravity driven eastward current that plays an important role in the development of these post midnight EPBs. Later, *Yizengaw et al*. [2013] demonstrated the existence of the RT instability during the post midnight hours using model studies. Even though, many of the above studies suggest RT instability as one of the key mechanism for the development of post midnight EPBs, the factors conducive for RT instability around the midnight hours were not clearly explained. In the present study, we investigated the nocturnal evolution of EPBs over Kototabang using EAR during 2011–2012. The responsible factors conducive for the development of summer time midnight EPBs were investigated by term-by-term analysis of flux tube integrated growth rate of RT instability using SAMI2 model simulations.

2. Data

The Equatorial Atmospheric Radar (EAR) at Kototabang, Indonesia (0.2°S geog. lat, 100.3°E geog. long, and 10.1°S dip. lat), operates at 47 MHz with a peak and average powers of 100 kW and 5 kW. During nighttime (18–06 LT) EAR is operated to observe the *F* region field aligned irregularities (FAIs) at ~3 m scale. Using the active phased array antenna system, it can steer the beam on a pulse-to-pulse basis. The rapid beam scanning ability enables the EAR to observe the temporal and spatial variations of backscatter plumes [*Fukao et al*., 2003]. In the present study, only the fresh and evolving-type EPBs observed over Kototabang during magnetically quiet periods of 2011–2012 were considered from the careful examination of their spatial and temporal evolution as explained in *Ajith et al*. [2015].

The vertical $E \times B$ drift velocities measured from the Ion Velocity Meter (IVM) on board the Communication/Navigation Outage Forecasting System (C/NOFS) satellite [*de La Beaujardière et al*., 2004] during 2011–2012 over 60–120° longitude were considered. The detailed description of the calibration of IVM is given by *Stoneback et al*. [2012]. The $E \times B$ drift velocity data derived from C/NOFS-IVM were fed to drive the SAMI2 model to reconstruct the background vertical electron density distributions and compute linear growth rate of RT instability. SAMI2 is a low-latitude ionospheric model, which models the plasma along the Earth's dipole magnetic field [*Huba et al*., 2000]. The model takes in to account of photoionization of neutrals and chemical evolution of seven ion species (H^+, He^+, N^+, O^+, N_2^+, NO^+, and O_2^+) in the altitude range 90–20,000 km. The ionospheric equations are solved along each field line using empirical models of neutral atmosphere NRLMSISE00 [*Picone et al*., 2002] for chemical reactions and HWM93 [*Hedin* et al., 1996] for thermospheric neutral winds.

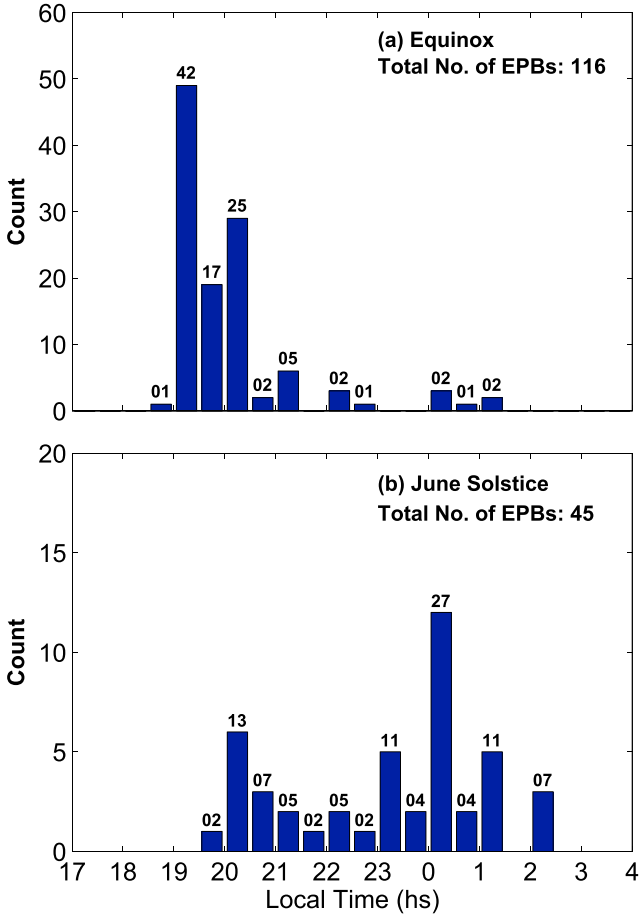

Figure 1. Histogram showing the nighttime occurrence of freshly evolved EPBs over Kototabang in (a) equinox and (b) June solstices during 2011–2012. The numbers shown on top of histogram bars indicate their percentages.

3. Results

It is well understood that the EPBs develop over magnetic equator, predominantly, during the post sunset hours of equinoxes [*Aarons et al*., 1980; *Yokoyama et al*., 2004]. Further, it is also reported in the previous studies that the EPB occurrence often increases around the midnight hours of June solstice, particularly, during the low solar active periods [*Otsuka et al*., 2009; *Yokoyama et al*., 2011; *Yizengaw et al*., 2013]. Hence, with a view to further examine the local time preferences of EPB development over Indonesian sector during equinox (March, April, September, and October) and June solstice (May, June, July, and August), only the plasma bubbles which are freshly originated and successively developed in the field of view of EAR were selected following the method of *Ajith et al*. [2015]. A total of 116 EPBs during equinox and 45 EPBs during June solstice was considered and binned in to 30 min intervals from 1700 to 0400 LT. Figures 1a and 1b show the nocturnal occurrence pattern of EPBs during 2011–2012 for equinox and June solstice, respectively. The numbers shown on top of each bin indicate their percentages. From Figure 1a, it is clear that the EPBs develop predominantly during the post sunset hours of equinoxes. Out of 116 EPBs during equinoxes, 68 EPBs (~59%) were evolved between 1900 and 2000 LT and 31 EPBs (~27%) during 2000–2100 LT. However, during June solstice, the nocturnal development pattern of EPBs is quite different from equinox as shown in Figure 1b. During June solstice, the EPB occurrence is significantly less compared to equinox at post sunset hours and the majority of EPBs (32 EPBs, i.e., ~71%) found to develop around and after midnight (2200–0300 LT).

From the previous studies, it is clear that the higher occurrence of EPBs during post sunset hours of equinox is associated with the post sunset height rise (PSSR) of equatorial *F* layer due to PRE [*Fejer et al*., 1999]. Further, it is also reported that the uplift of *F* layer is responsible for the development of EPBs around midnight of June solstice as well [e.g., *Nishioka et al*., 2012; *Ajith et al*., 2015]. Hence, in order to understand the *F* layer height elevation and the background zonal electric field variation during midnight hours, the vertical E × B drift velocity data from IVM on board C/NOFS satellite was analyzed. The E × B drift velocities in our analysis are taken within ±10° latitudes centered on magnetic equator over 60–120° longitudes during 2011–2012. The days with $Kp > 3$ were excluded to restrict the data to periods of low geomagnetic activity. To ensure the accuracy of the velocity measurements the satellite altitude is limited to 400–550 km and a lower limit for the O^+ concentration of $3 \times 10^3\,cm^{-3}$ is maintained similar to *Stoneback et al*. [2011]. Finally, the E × B drift velocities are averaged for each 30 min local time interval from 1700 to 0400 LT. The mean E × B drift velocity calculated separately for equinox (March, April, September, and October) and June Solstice (May, June, July, and August) and its local time variations are presented in Figures 2a and 2b, respectively. The thick black curve in Figure 2 shows the mean drift velocity, and the standard deviation is represented by error bars. From Figure 2a, it is clear that during

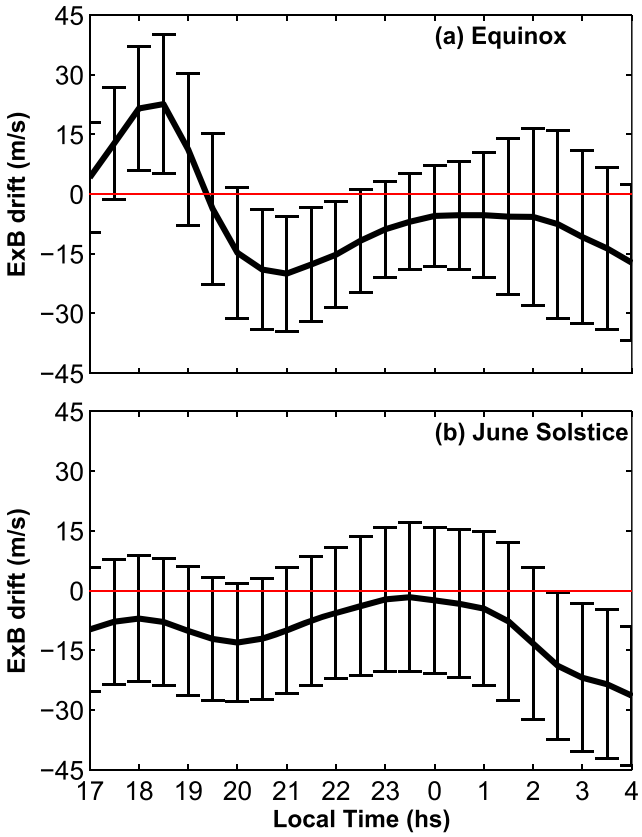

Figure 2. The mean E × B drift variation for (a) equinox and (b) June solstice obtained from IVM on board C/NOFS satellite during 2011–2012.

post sunset hours of equinox, the E × B drift is largely positive (upward) and reaching a maximum of 22.6 m/s around 1830 LT representing the well-known PRE effect. After reaching the peak value, E × B drift velocity quickly decreases and become negative (downward) around 1930 LT with a maximum downward velocity of −20.0 m/s around 2100 LT. The E × B drift slightly recovers at later times, however, remains downward throughout the night. From Figures 1a and 2a, the large post sunset vertical drifts due to PRE explain the higher occurrence of EPBs during the post sunset hours of equinox. On the other hand, PRE is almost absent in June solstice and E × B drift is downward with a minimum of −13.1 m/s at 2000 LT as shown in Figure 2b. Further, it is interesting to observe that E × B drift starts increasing around 2100 LT and exhibits broad peak between 2200 and 0200 LT with a maximum value of −1.7 m/s around 2330 LT. This weak westward electric field around the midnight hours of June solstice from C/NOFS observations is consistent with the earlier observations by *Fejer et al*. [1991]. Thus, enhanced development of EPBs during the midnight hours (2200–0300 LT) of June solstice (Figures 1b and 2b) could be due to the presence of weaker westward electric fields.

3.1. SAMI2 Model Calculations

As mentioned earlier, the elevated equatorial *F* layer is playing an important role in the development of EPBs around midnight. However, the mechanism which causes the uplift of *F* layer during this period is not yet understood well. Several processes can contribute to the *F* layer height rise during midnight over equator and low-latitude regions. For example, the enhanced equatorward wind around midnight over Indonesian sector [*Maruyama et al*., 2008] can drag the plasma toward the equator from off-equatorial latitudes and maintain at higher altitudes over equator. Further, due to the weak westward electric field (Figure 2b), the downward drift of *F* region plasma is negligible and the *F* layer remains at higher altitude. Another process that can cause the apparent vertical drift of *F* layer is the recombination of bottomside plasma during nighttime. Thus, the influence of these weaker westward electric fields in the presence of enhanced equatorward wind and bottomside recombination on the uplift of *F* layer and development of EPBs around and after midnight hours of June solstice need to be investigated. Hence, we employed SAMI2 model to obtain the background vertical electron density distribution under the conditions of mean E × B drift velocities shown in Figure 2. In the present study, our objective is to examine the possibility of EPB development under the influence of weakly westward electric field around the midnight hours of June solstice as shown in Figure 2b. Therefore, in the present SAMI2 model simulation, we considered only the mean E × B drift curve from Figure 2 (ignoring the scatter indicated by the error bars) as an input to model. The model simulation is carried out under the moderate solar activity conditions ($F_{10.7}$ cm solar flux = 100 solar flux unit) over EAR longitudinal (100.32°E) sector for day numbers 80 (representing equinox) and 172 (representing June solstice). Figure 3 shows the vertical electron density distribution over dip equator from the SAMI2 model simulations as a function of local time for equinox (Figure 3a) and June solstice (Figure 3b). The white curves in Figures 3a and 3b indicate the mean E × B drift velocity variations obtained from CINDI-IVM (shown in Figure 2) that fed

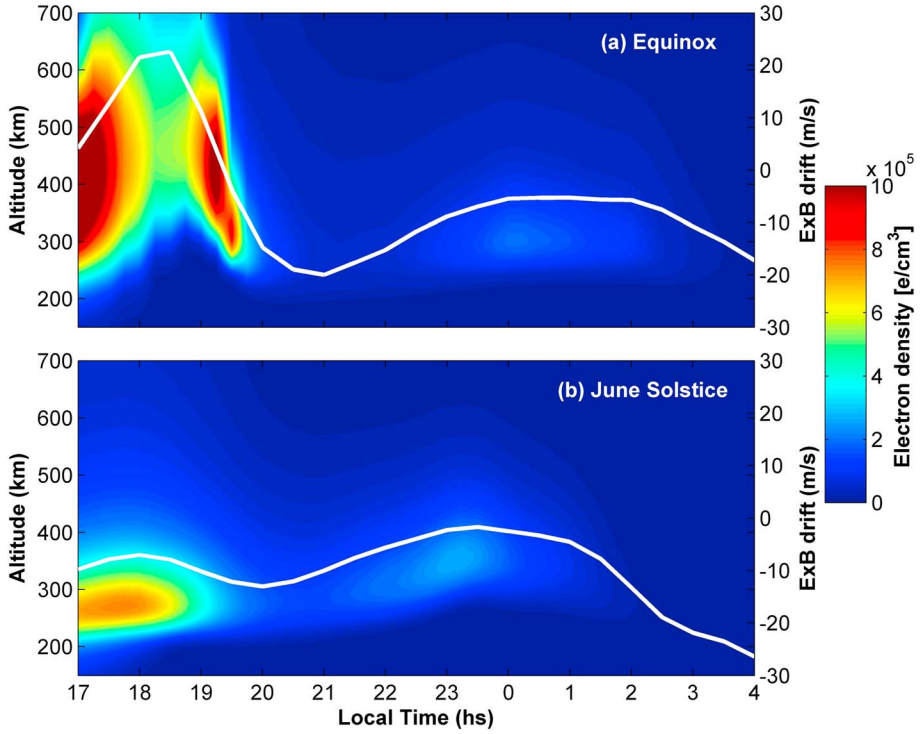

Figure 3. The altitude-local time distributions of ionospheric electron density over magnetic equator derived from SAMI2 Model for (a) day no. 80 (equinoctial day) and (b) day no. 172 (June solstice day). The white curve shows the mean E × B drift velocity derived from CINDI IVM observations on board C/NOFS satellite.

to the model. It can be observed from Figure 3a, during equinoxes, the *F* layer is elevated to higher altitudes with increasing E × B drift velocity and reaches maximum height around 1830 LT. Further, it can be seen that during the post sunset hours (~1800–1830 LT) electron density is relatively less and distributed over a large altitudinal range (~300–700 km) because of the vertical transport of plasma via equatorial fountain process due to PRE. This redistribution of *F* layer plasma due to large upward E × B drift results in small vertical density gradients in *F* region during this period (1800–1830 LT). After reaching a maximum altitude at 1830 LT, *F* layer is started to descend due to decrease in upward E × B drift. During this descending period, the *F* layer contracts in altitude due to the quick decrease of upward E × B drift which results in a steep vertical density gradient at the bottomside *F* layer around 1830–2000 LT. As the time progresses, the *F* layer descends to lower altitudes with the reversal of E × B drift and the electron density become small due to recombination. Further, during late night hours, the *F* layer is slightly elevated in response to small recovery in E × B drift.

In case of June solstice, *F* layer does not exhibit height rise during post sunset hours because of the absence of PRE and overall electron density is much lesser than equinox (Figure 3b). The bottom height of *F* layer is around 200 km during the post sunset hours and as time progresses the *F* layer height increases around midnight hours. Further, it is interesting to observe that a noticeably enhanced density region with significant vertical density gradient is developed at the altitude ~300-400 km around 2200–0200 LT. It can be noticed from Figure 3b that the input E × B drift is not upward; however, it is weakly downward during this period. Hence, the uplift of equatorial *F* layer is not necessarily due to eastward zonal electric field. Due to this weak westward electric field, the downward drift of *F* layer is generally weak during these local times in June solstice that keeps the *F* region plasma at relatively higher altitudes. Figure 4 shows the meridional neutral wind (positive northward) along EAR longitude (100.32°) around 200 km altitude from HWM93 model as a function of geographic latitude and local time for June solstice, which inputs to the SAMI2 model. It can be seen from Figure 4 that the equatorward neutral wind is enhanced at low latitudes of both hemispheres during 2200–0200 LT. *Maruyama et al.* [2008] have also reported the enhanced equatorward neutral winds during this period over Indonesian sector using the low-latitude meridional chain of ionosonde observations. The enhanced equatorward meridional wind during this period can drag the plasma along the field lines from off-equatorial region to the higher altitudes over equatorial region. In addition, the bottomside recombination of plasma,

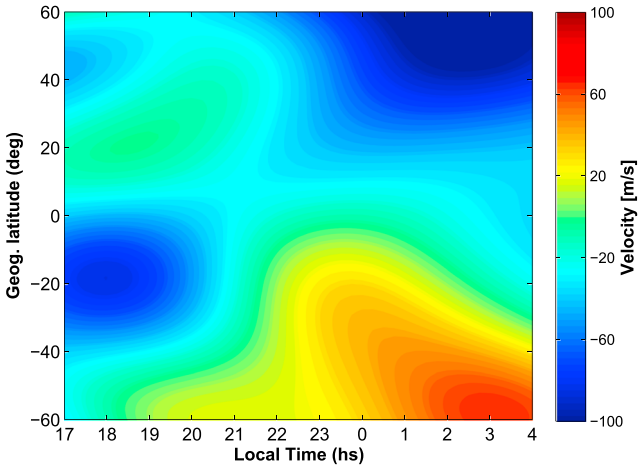

Figure 4. The meridional neutral wind (positive northward) as a function of geographic latitude and local time along Indonesian sector (EAR longitudes) at 200 km altitude for day number 172.

particularly, when the *F* layer heights are below 300 km [*Bittencourt and Abdu*, 1981] causes an apparent uplift of *F* layer. Using model simulation, *Nicolls et al*. [2006] have shown that bottomside recombination is an important factor for the *F* layer uplift when the westward electric field is weak. Hence, the results observed from Figure 3b shows that weaker westward electric fields in the presence of bottomside recombination and enhanced equatorward meridional wind play important role for the uplift of *F* layer and formation of enhanced density region with significant vertical gradient around the midnight hours of June solstice.

In order to see the influence of such vertical electron density distributions shown in Figures 3a and 3b, on the development of EPBs during equinoxes and June solstices, respectively, the flux tube integrated linear growth rate of RT instability is computed by estimating the individual terms of growth rate equation given by *Sultan* [1996] as

$$\gamma_{\mathrm{RT}} = \frac{\Sigma_P^F}{\Sigma_P^F + \Sigma_P^E}\left(V_P - U_L^P - \frac{g_e}{\nu_{eff}^F}\right)K^F - R_T, \tag{1}$$

where Σ_P^F and Σ_P^E are the flux tube integrated *F* region and *E* region Pedersen conductivities, respectively. V_P is the upward drift speed taken from the mean drift curve obtained from CINDI-IVM as shown in Figure 2. U_L^P is the flux tube integrated neutral wind perpendicular to the field line weighted by the Pedersen conductivity calculated using HWM model.

The flux tube integrated effective *F* region collision frequency (ν_{eff}^F) is computed by the flux tube integration of local ion-neutral collision frequency given by *Kelley* [1989],

$$\nu_{\mathrm{in}} = 2.6\times10^{-9}(n_n + n)A^{-1/2}, \tag{2}$$

where n_n is the neutral density and A is the mean neutral molecular mass in atomic mass units. The $K^F = \frac{1}{N_e}\left(\frac{\partial N_e}{\partial h}\right)$ is the vertical gradient of the field line integrated electron content in the *F* region, N_e is the flux tube electron content, and R_T is the flux tube integrated recombination rate, which is assumed to be n egligible in the present study.

Following *Sultan* [1996], the flux tube integrated parameters in the RT instability growth rate equation is estimated by an integration of local values from an altitude of 125 km in one hemisphere to 125 km in the opposite hemisphere along the magnetic flux tubes. The integration is performed separately for a series of flux tubes up to an apex altitude of 1000 km. The boundary between *E* and *F* layer was chosen to be 200 km for the calculation of Pederson conductivities. The *E* and *F* region Pedersen conductivities are obtained by the field line integration of local Pedersen conductivity given as

$$\sigma_p = \frac{ne}{B}\left(\frac{K_i}{1+K_i^2} - \frac{K_e}{1+K_e^2}\right) \tag{3}$$

where n is the electron density, e is the elementary charge, B is the magnetic field, and K_i and K_e are the ratios of the gyro frequency to collision frequency for ions and electrons, respectively.

The altitudinal and local time variations of the *F* region flux tube electron content height gradient (K^F) (a, b), flux tube integrated effective *F* region collision frequency (ν_{eff}^F) (c, d), and the flux tube integrated linear growth rate for RT instability (γ_{RT}) (e, f) are presented in Figure 5. Figures 5a, 5c, and 5e are for the equinoctial day (day no. 80) and Figures 5b, 5d, and 5f are for June solstice day (day no. 172). An important feature that

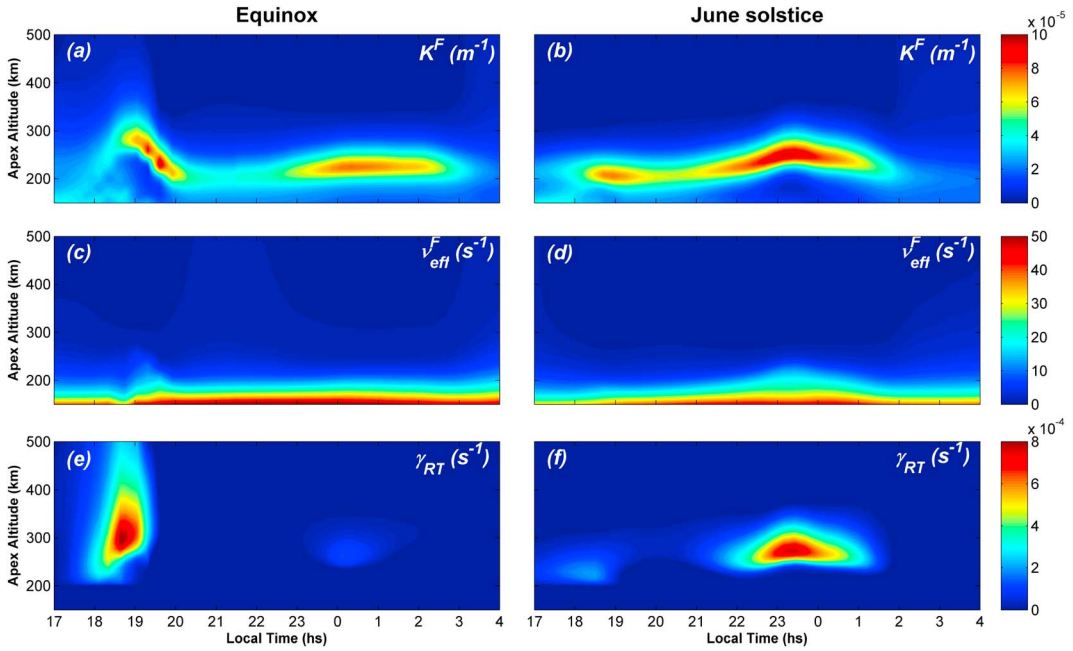

Figure 5. Altitude-local time variations of (a, b) *F* region flux tube electron content height gradient (K^F), (c, d) flux tube integrated effective *F* region collision frequency (ν^F_{eff}), and (e, f) the flux tube integrated linear growth rate for RT instability (γ_{RT}) for equinox (Figures 5a, 5c, and 5e) and June solstice (Figures 5b, 5d, and 5f), respectively.

can be noted from Figure 5a is that the steep vertical density gradient region forms at an altitude of ~250–300 km and K^F reaches its maximum value during 1830–1930 LT when the E × B drift starts decreasing (Figures 2a and 3a). This steep gradient (high K^F) region descends to lower altitudes (~200 km) with the decrease in E × B drift and disappears by ~2000 LT with reversal of E × B drift. During the June solstice period (Figure 5b), the K^F reaches a value of $\sim 7 \times 10^{-5}\,m^{-1}$ around 1830–1930 LT, however, at a lower altitude of ~200 km due to the absence of PRE. The K^F starts increasing again from 2100 LT, and the steep gradient region is gradually ascending with time reaching a peak altitude of ~250–300 km with a maximum value of $\sim 10 \times 10^{-5}\,m^{-1}$ around 2300 LT.

4. Discussions

The EPBs in the nightside ionosphere generally develop at magnetic equator under RT instability. Using the Advanced Research Project Agency (ARPA) Long-range Tracking and Identification Radar (ALTAIR) data set, *Sultan* [1996] correlated the RT instability growth rate with Equatorial Spread-F (ESF) occurrence and shows good agreement. Later, *Carter et al.* [2014] studied the relation between RT instability growth rate and EPB occurrence over the Southeast Asian longitudes and showed good correlation. During equinox, the steep vertical density gradient (high K^F) region is formed around ~1830–1930 LT when the E × B drift starts decreasing (Figure 5a). This high K^F can be explained as follows. During the peak E × B drift period, *F* region plasma is vertically transported to topside ionosphere and distributed over large altitude range via equatorial fountain process; hence, the bottomside vertical density gradient becomes minimum. However, the *F* layer contracts in altitude when the E × B drift is decreasing that result in a steep vertical density gradient at the bottomside *F* layer as can be seen from Figure 3a. Further, at time of E × B drift reversal, reverse fountain effect [*Sridharan et al.*, 1993] will play a major role to keep the density high over equator. Under the effect of downward E × B drift, the plasma in the topside *F* region around the equator is pushed downward across the magnetic field lines and creates a low plasma region in the topside ionosphere. Plasma flows toward equator from low latitudes to fill this low-pressure region and again pushed downward across the magnetic field lines [*Balan and Bailey*, 1995]. This process results higher plasma density around equator and steep vertical density gradient at the bottomside of *F* region near the time of drift reversal. This steep vertical density gradient (high K^F) region at relatively higher altitude region of ~250–300 km during 1830 to 1930 LT causes enhanced growth rate (γ_{RT}) as shown in Figure 5e that sets the most favorable conditions for the development of EPBs during equinoxes.

This result shows good agreement with the previous studies, which reported that the plasma bubbles usually develop at the bottomside *F* region around the time of reversal of E × B drift [*Rastogi*, 1980; *Abdu et al*., 1982; *Fejer et al*., 1999]. Using Jicamarca radar observations, *Farley et al*. [1970] suggested that the high altitude obtained by *F* layer is more important for the onset of spread *F* than the upward velocity of *F* layer during onset time. Later, *Fejer et al*. [1999] observed that spread *F* irregularities are generated close to the time of reversal of evening drift velocity and they suggested that the evolution of spread *F* during this period is a race against time where the irregularities in the low altitude layers are developed and rise in to the topside layer under the influence of polarization electric fields, before they are damped as a result of large downward drift. This higher growth rate during the post sunset hours will explain the higher occurrence of evolving-type EPBs during the equinoxes observed by EAR (Figure 1a).

However, one can observe from Figure 1a that a significant number of EPBs (27%) found to develop at local times between 2000 and 2100 LT where the growth rate (γ_{RT}) obtained from SAMI2 simulation is negligibly small (Figure 5e). This could be due to the fact that an EPB takes a finite rise time, ~10–50 min [e.g., *Dao et al*., 2016], from its onset at bottomside *F* region over equator and grow altitudinally to ~400 km to map along field lines so as to be detected by EAR at an off-equatorial (10° dip. lat) location. Further, Figure 5e represents the model simulation for a particular day (day no. 80) assuming that the mean E × B drift variation shown in Figure 2a, the day-to-day variability of E × B drift, and post sunset height rise were not accounted in the current model simulation. The K^F again increases around 2300 LT and reaches to a value of $\sim 7 \times 10^{-5}$ m^{-1}, however, at altitudes below 240 km. The relatively low value of K^F and high value of ν_{eff}^F (Figure 5c) at these altitudes make growth rate (γ_{RT}) insufficient for the development of EPBs around the midnight hours of equinoxes.

The interesting point that should be noted from Figure 5b is that during June solstice the steep vertical density gradient (high K^F) region around midnight hours is present at a higher altitude where the ion-neutral collision frequency is significantly small. From Figure 5d, it can be seen that ν_{eff}^F decreases exponentially with increasing altitude. The decrease in ν_{eff}^F with altitude causes increase in the growth rate (γ_{RT}) when the high K^F region is elevated to higher altitude as can be seen from Figures 5b and 5f. Further, the estimated linear growth rate (γ_{RT}) is sufficiently high during 2200–0200 LT (Figure 5f) that can explain the onset and development of EPBs around midnight hours observed from EAR over Indonesian sector (Figure 1b) during June solstice. Hence, the results from this study confirm the role of RT instability behind the fresh development of EPBs around midnight as suggested by the previous studies [*Yokoyama et al*., 2011; *Nishioka et al*., 2012; *Yizengaw et al*., 2013] through model simulations. It may also be mentioned that there are sufficient number of EPBs observed during 2000–2100 LT of June solstice where the growth rate obtained from SAMI2 simulation is negligibly small. The mechanism behind the occurrence of these EPBs over Indonesian sector is not clear, and these cases needed to be studied in case-by-case basis. The model simulation of growth rate indicates the mean variation representing for June solstice, and there could be a large day-to-day variability in the controlling factors such as *F* layer height, E × B drift, and neutral winds that may cause inconsistency between the actual observation from EAR and growth rate obtained from model simulation.

In order to see the effects of equatorward neutral wind and weaker westward zonal electric field, separately, on the uplift of *F* layer and enhanced growth rate of RT instability around the midnight hours of June solstice, two cases of controlled SAMI2 simulations were carried out. In first case, the meridional neutral wind input to SAMI2 model is turned off and the model simulation is carried out for day number 172 with input E × B drift estimated for June solstice. In second case, the SAMI2 model is run by turning off neutral wind and modified mean E × B drift with significant down ward drift of −6 m/s between 2200 and 0100 LT.

4.1. Case I

In order to see the neutral wind effect on the elevation of *F* layer, the SAMI2 simulation is carried out without neutral wind input. Figure 6 shows the flux tube electron content height gradient (K^F) (Figure 6a) and the linear growth rate of RT instability (γ_{RT}) (Figure 6b) as a function of local time and apex altitude obtained for June solstice with neutral wind set to 0 m/s. It can be seen from Figure 6a that a steep density gradient region is formed between 2200 and 0100 LT similar to Figure 5b but comparatively at lower altitude (~210–260 km). Further, it can also be seen from Figure 6b that the flux tube integrated linear growth rate of RT instability

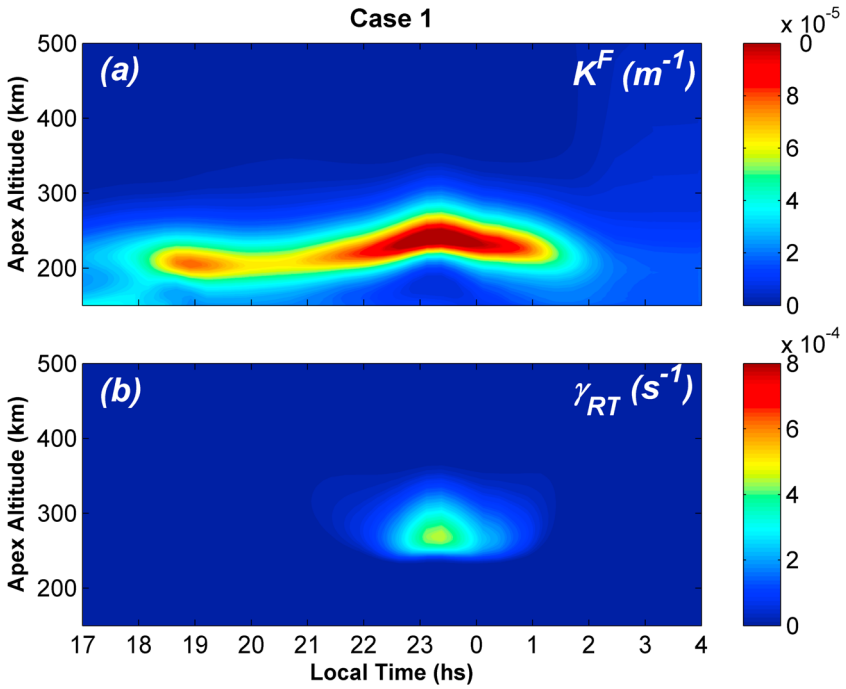

Figure 6. Altitude-local time variations of (a) *F* region flux tube electron content height gradient (K^F) and (b) the flux tube integrated linear growth rate for RT instability (γ_{RT}) for June solstice (day no. 172) estimated using SAMI2 model simulation with neutral wind input turned off.

is significantly reduced compared to the case when the neutral wind is included (Figure 5f). The lower altitude of steep vertical gradient (high K^F) region resulted in the reduced growth rate when the neutral wind is turned off (Figure 6).

4.2. Case 2

In this case, the mean E × B drift around and after the midnight period of June solstice is modified with a downward drift of −6 m/s during 2200–0100 LT. SAMI2 model is run with this modified E × B drift input and neutral wind turned off for day number 172. The flux tube electron content height gradient (K^F) and linear growth rate of RT instability (γ_{RT}) estimated from this controlled simulation are presented in Figures 7a and 7b, respectively. The white curve in Figure 7a represents the modified mean E × B drift velocity that fed to the model. It can be noticed from Figure 7a that with the modified E × B drift of −6 m/s, the steep vertical gradient (high K^F) region is formed at lower altitudes (~190–230 km) and the growth rate (γ_{RT}) is greatly reduced to $\sim 5 \times 10^{-5}\ s^{-1}$ (Figure 7b, note the change in color scale). This clearly indicates that the growth rate reduces substantially when the westward zonal electric field is significant. Hence, the presence of weaker westward electric fields around midnight of June solstices allows the formation of high K^F (steep gradient) region at relatively higher altitudes and causes enhanced growth rate of RT instability.

Ajith et al. [2015] and *Dao et al*. [2016] have shown the initial altitudes of EPB onset observed from EAR are significantly smaller during post midnight periods compared to post sunset hours. The higher initial altitudes of post sunset EPBs are due to rapid uplift of equatorial *F* layer during PRE. However, the elevation of equatorial *F* layer around midnight hours of June solstices is small compared to PSSR during equinoxes. Thus, in order to see the necessary height rise for the onset of EPBs around the midnight period of June solstice compared to post sunset hours of equinox, the altitudinal profiles of linear growth rate of RT instability for equinox at 1900 LT (green) and June solstice at 2330 LT (black) were compared as shown in Figure 8. It can be observed from this figure that a given growth rate (γ_{RT}) could be achieved at lower altitude around the midnight hours of June solstice compared to post sunset hours of equinox. For example, a growth rate of $7.8 \times 10^{-4}\ s^{-1}$ is attained at an altitude of 295 km (double headed green arrow) during equinox at 1900 LT; however, the same growth rate is attained even at a lower altitude of 270 km (double headed black arrow) at

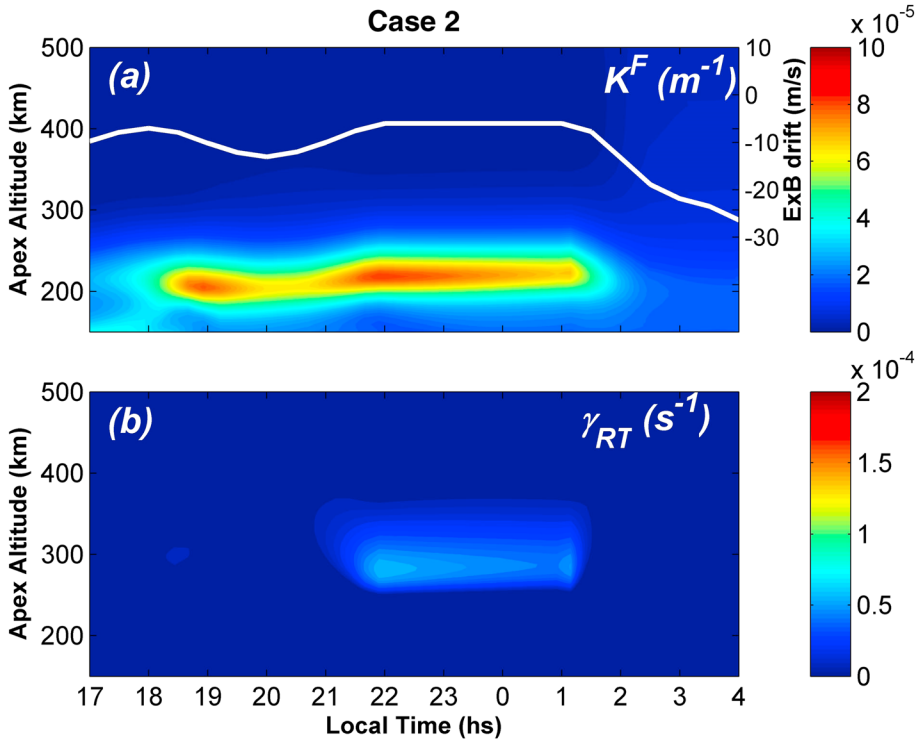

Figure 7. Altitude-local time variations of (a) *F* region flux tube electron content height gradient (K^F) and (b) the flux tube integrated linear growth rate for RT instability (γ_{RT}) for June solstice (day no. 172) estimated using SAMI2 model simulation with neutral wind input turned off and introducing downward E × B drift of −6 m/s during 2200–0100 LT. The white curve in Figure 7a shows the modified E × B drift input that fed to the model.

2330 LT during June solstice. This result indicates that a bubble can initiate even at a lower altitude around the midnight hours of June solstice than the post sunset hours of equinoxes.

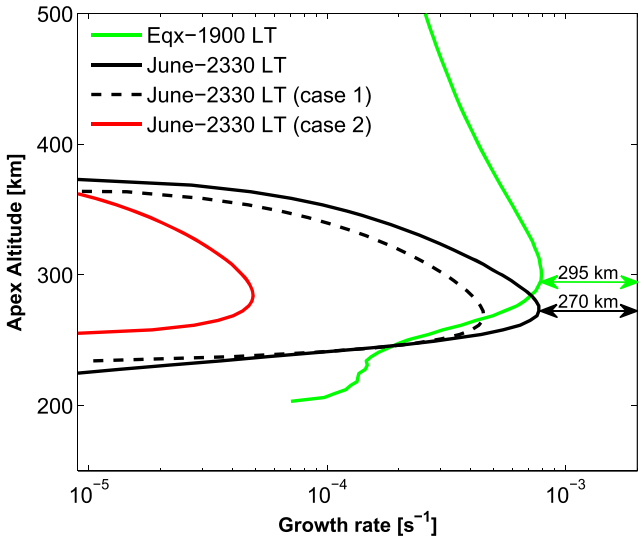

Figure 8. The altitudinal profile of flux tube integrated growth rate of collisional Rayleigh-Taylor instability. The green and black solid curves represent the 1900 LT of equinox and 2330 LT of June solstices, respectively. The black dotted curve represents the case for June solstice with neutral wind input turned off (case 1). The red curve represents the case for June solstice with a downward E × B drift of −6 m/s (case 2).

The black dotted curve in Figure 8 represents the growth rate of June solstice for the case with neutral wind turned off (case 1), and red curve represents the growth rate for the case with modified E × B drift (case 2). It can be seen from Figure 8 that the growth rate at 2330 LT of June solstice is maximum (7.8×10^{-4} s^{-1}) with neutral wind effects included in the presence of weaker westward electric fields (black solid curve). The peak growth rate is decreased to 4.5×10^{-4} s^{-1} when the neutral wind is turned off (black dotted curve). Further, the growth rate is substantially decreased (by more than one order) to 4.8×10^{-5} s^{-1} when the downward E × B drift of −6 m/s introduced (red curve). Therefore, the results presented in Figures 6 to 8 clearly indicate that the enhanced linear growth rate and occurrence of EPBs during midnight hours of June solstice are mainly

due to the presence of relatively weaker westward electric fields with a smaller contribution from the equatorward meridional neutral wind.

In the present study, we examined the background ionospheric conditions for the onset of EPBs by estimating the flux tube integrated linear growth rate of RT instability. It should be mentioned here that the linear growth rate estimated in this study indicates the initial growth of the EPBs during the time of onset at the bottomside of *F* region. Once initiated, the EPB can grow vertically up to an altitude where the ambient density becomes equal to the density inside the bubble. The altitudinal development and further nonlinear expansion of EPBs depend on several factors like ambient density, zonal electric filed, and thermospheric neutral winds. During the post sunset hours of equinox, in the presence of strong eastward electric field the EPBs can grow rapidly to higher altitudes with larger vertical rise velocities [*Dao et al*., 2016]. However, around the midnight periods of June solstice, even though the elevated *F* layer and high K^F results in the significant initial growth rate, the weak westward electric field will slow down the growth of EPB development and suppress the EPBs before growing to higher altitudes. This could be the reason for less number of EPBs, slower rise velocities, and lower altitude confinement of EPBs [*Dao et al*., 2016] observed around the midnight hours of June solstice compared to the post sunset hours of equinox.

5. Conclusions

We have analyzed the nighttime development of freshly evolved EPBs over Kototabang using the rapid beam steering facility of EAR during the moderate solar active years 2011–2012. Out of 116 EPBs during equinoxes, 99 EPBs (~85%) were found to evolve during the post sunset hours (1900–2100 LT). However during June solstice, the majority of EPBs (32 EPBs, i.e., ~71%) found to develop around midnight between 2200 and 0300 LT. The physics-based SAMI2 model is employed to simulate the background electron density distributions for equinox and June solstices with a realistic E × B input derived from CINDI IVM observations on board C/NOFS satellite. The altitudinal and local time variations of flux tube integrated electron content height gradient (K^F), effective *F* region collision frequency (ν^F_{eff}) and growth rate of RT instability (γ_{RT}) were modeled separately for both equinox and June solstice conditions. The results show that the growth rate is maximized during the post sunset hours in equinox and around midnight hours in June solstice, which corresponds well with the maximum occurrence of EPBs observed by EAR. The elevated equatorial *F* layer and formation of high K^F layer at higher altitudes found to be the key factors for enhanced growth rate of RT instability around the midnight hours of June solstices. The responsible factors are discussed in terms of relatively weaker westward zonal electric fields around midnight of June in the presence of equatorward neutral wind and bottomside recombination. The case controlled SAMI2 model simulations indicate that the enhanced growth rate and the development of EPBs around the midnight hours of June are more likely due to the weaker westward electric fields with a smaller contribution from the equatorward neutral wind. Further, it is observed that a given growth rate (γ_{RT}) can be achieved at a lower altitude during the midnight hours of June solstice compared to post sunset period of equinox. This study confirms the role RT instability on the development of summertime EPBs around the midnight hours over Indonesian sector.

Acknowledgments
The work of S.T.R. is partly supported by STEL joint international research program 2015 and Department of Science and Technology, Government of India through India-Taiwan Science and Technology, project GITA/DST/TWN/P-47/2013. The EAR data obtained from the PI, M. Yamamoto (yamamoto@rish.kyoto-u.ac.jp). The CINDI-IVM data are provided through the auspices of the CINDI team at the University of Texas at Dallas supported by NASA grant NAS5-01068 (http://cda-web.gsfc.nasa.gov/cgi-bin/eval1.cgi).

References

Aarons, J., J. P. Mullen, H. E. Whitney, and E. M. Mackenzie (1980), The dynamics of equatorial irregularity patch formation, motion and decay, *J. Geophys. Res.*, *85*, 139–149, doi:10.1029/JA085iA01p00139.

Abdu, M. A., J. A. Bittencourt, and I. S. Batista (1981), Magnetic declination control of the equatorial *F* region dynamo electric field development and spread *F*, *J. Geophys. Res.*, *86*, 11,443–11,446, doi:10.1029/JA086iA13p11443.

Abdu, M. A., R. T. De Medeiros, and J. H. A. Sobral (1982), Equatorial spread *F* instability conditions as determined from ionograms, *Geophys. Res. Lett.*, *9*(692), 692–695, doi:10.1029/GL009i006p00692.

Ajith, K. K., S. Tulasi Ram, M. Yamamoto, T. Yokoyama, V. S. Gowtam, Y. Otsuka, T. Tsugawa, and K. Niranjan (2015), Explicit characteristics of evolutionary-type plasma bubbles observed from Equatorial Atmosphere Radar during the low to moderate solar activity years 2010–2012, *J. Geophys. Res. Space Physics*, *120*, 1371–1382, doi:10.1002/2014JA020878.

Balan, N., and G. J. Bailey (1995), Equatorial plasma fountain and its effects: Possibility of an additional layer, *J. Geophys. Res.*, *100*, 21,421–21,432, doi:10.1029/95JA01555.

Bittencourt, J. A., and M. A. Abdu (1981), A theoretical comparison between apparent and real vertical ionization drift velocities in the equatorial F region, *J. Geophys. Res.*, *86*(A4), 2451–2454, doi:10.1029/JA086iA04p02451.

Bhattacharyya, A., S. Basu, K. M. Groves, C. E. Valladares, and R. Sheehan (2001), Dynamics of equatorial F region irregularities from spaced receiver scintillation observations, *Geophys. Res. Lett.*, *28*(1), 119–122, doi:10.1029/2000GL012288.

Carter, B. A., E. Yizengaw, J. M. Retterer, M. Francis, M. Terkildsen, R. Marshall, R. Norman, and K. Zhang (2014), An analysis of the quiet time day-to-day variability in the formation of postsunset equatorial plasma bubbles in the Southeast Asian region, *J. Geophys. Res. Space Physics*, *119*, 3206–3223, doi:10.1002/2013JA019570.

Dao, E., M. C. Kelley, P. Roddy, J. Retterer, J. O. Ballenthin, O. de La Beaujardiere, and Y.-J. Su (2011), Longitudinal and seasonal dependence of nighttime equatorial plasma density irregularities during solar minimum detected on the C/NOFS satellite, *Geophys. Res. Lett.*, *38*, L10104, doi:10.1029/2011GL047046.

Dao, T., Y. Otsuka, K. Shiokawa, S. Tulasi Ram, and M. Yamamoto (2016), Altitude development of postmidnight *F* region field-aligned irregularities observed using Equatorial Atmosphere Radar in Indonesia, *Geophys. Res. Lett.*, *43*, 1015–1022, doi:10.1002/2015GL067432.

de La Beaujardière, O., et al. (2004), C/NOFS: A mission to forecast scintillations, *J. Atmos. Sol. Terr. Phys.*, *66*, 1573–1591, doi:10.1016/j.jastp.2004.07.030.

Farley, D. T., B. B. Balsley, R. F. Woodman, and J. P. Mc-Clure (1970), Equatorial spread-*F*: Implications of VHF radar observations, *J. Geophys. Res.*, *75*, 7199–7216, doi:10.1029/JA075i034p07199.

Farley, D. T., E. Bonelli, B. G. Fejer, and M. F. Larsen (1986), The prereversal enhancement of the zonal electric field in the equatorial ionosphere. *J. Geophys. Res. 91*, 13,723–13,728.

Fejer, B. G., E. R. de Paula, S. A. Gonzalez, and R. F. Woodman (1991), Average vertical and zonal *F* region plasma drifts over Jicamarca, *J. Geophys. Res.*, *96*(A8), 13,901–13,906, doi:10.1029/91JA01171.

Fejer, B. G., L. Scherliess, and E. R. de Paula (1999), Effects of the vertical plasma drift velocity on the generation and evolution of equatorial spread *F*, *J. Geophys. Res.*, *104*(A9), 19,859–19,869, doi:10.1029/1999JA900271.

Fukao, S., H. Hashiguchi, M. Yamamoto, T. Tsuda, T. Nakamura, M. K. Yamamoto, T. Sato, M. Hagio, and Y. Yabugaki (2003), Equatorial Atmosphere Radar (EAR): System description and first results, *Radio Sci.*, *38*(3), 1053, doi:10.1029/2002RS002767.

Hedin, A. E., et al. (1996), Empirical wind model for the upper, middle and lower atmosphere, *J. Atmos. Terr. Phys.*, *58*, 1421–1447, doi:10.1016/0021-9169(95)00122-0.

Heelis, R. A., R. Stoneback, G. D. Earle, R. A. Haaser, and M. A. Abdu (2010), Medium-scale equatorial plasma irregularities observed by Coupled Ion-Neutral Dynamics Investigation sensors aboard the Communication Navigation Outage Forecast System in a prolonged solar minimum, *J. Geophys. Res.*, *115*, A10321, doi:10.1029/2010JA015596.

Huba, J. D., G. Joyce, and J. A. Fedder (2000), Sami2 is another model of the ionosphere (SAMI2), A new low-latitude ionosphere model, *J. Geophys. Res.*, *105*, 23,035–23,053, doi:10.1029/2000JA000035.

Kelley, M. C. (1989), *The Earth's Ionosphere*, *Int. Geophys. Ser.*, vol. 43, Elsevier, New York.

Krishna Moorthy, K., C. Ragha Reddi, and B. V. Krishna Murthy (1979), Night time ionospheric scintillations at the magnetic equator, *J. Atmos. Terr. Phys*, *41*, 123–134, doi:10.1016/0021-9169(79)90004-7.

Maruyama, T., S. Saito, M. Kawamura, and K. Nozaki (2008), Thermospheric meridional winds as deduced from ionosonde chain at low and equatorial latitudes and their connection with midnight temperature maximum, *J. Geophys. Res.*, *113*, A09316, doi:10.1029/2008JA013031.

Nicolls, M. J., M. C. Kelley, M. N. Vlasov, Y. Sahai, J. L. Chau, D. L. Hysell, P. R. Fagundes, F. Becker-Guedes, and W. L. C. Lima (2006), Observations and modeling of post-midnight uplifts near the magnetic equator, *Ann. Geophys.*, *24*, 1317–1331, doi:10.5194/angeo-24-1317-2006.

Nishioka, M., Y. Otsuka, K. Shiokawa, T. Tsugawa, Effendy, P. Supnithi, T. Nagatsuma, and K. T. Murata (2012), On post-midnight field-aligned irregularities observed with a 30.8-MHz radar at a low latitude: Comparison with *F*-layer altitude near the geomagnetic equator, *J. Geophys. Res.*, *117*, A08337, doi:10.1029/2012JA017692.

Otsuka, Y., T. Ogawa, and Effendy (2009), VHF radar observations of night time *F*-region field-aligned irregularities over Kototabang, Indonesia, *Earth Planets Space*, *61*, 431–437, doi:10.1186/BF03353159.

Picone, J. M., A. E. Hedin, D. P. Drob, and A. C. Aikin (2002), NRLMSISE-00 empirical model of the atmosphere: Statistical comparisons and scientific issues, *J. Geophys. Res.*, *107*(A12), 1468, doi:10.1029/2002JA009430.

Rama Rao, P. V. S., S. Tulasi Ram, K. Niranjan, D. S. V. V. D. Prasad, S. Gopikrishna, and N. K. M. Lakshmi (2005), VHF and L-band scintillation characteristics over Indian low-latitude station, Waltair, *Ann. Geophys.*, *23*, 2457–2464, doi:10.5194/angeo-23-2457-2005.

Rastogi, R. G. (1980), Seasonal and solar cycle variations of equatorial spread *F* in the American zone, *J. Atmos. Terr. Phys.*, *42*, 593.

Sastri, J. H. (1999), Post-midnight onset of spread-*F* at Kodaikanal during the June solstice of solar minimum, *Ann. Geophys.*, *17*, 1111–1115.

Sridharan, R., R. Sekar, and S. Gurubaran (1993), Two-dimensional high resolution imaging of the equatorial plasma fountain, *J. Atmos. Terr. Phys.*, *55*, 1661–1663, doi:10.1016/0021-9169(93)90170-4.

Stoneback, R. A., R. A. Heelis, A. G. Burrell, W. R. Coley, B. G. Fejer, and E. Pacheco (2011), Observations of quiet time vertical ion drift in the equatorial ionosphere during the solar minimum period of 2009, *J. Geophys. Res.*, *116*, A12327, doi:10.1029/2011JA016712.

Stoneback, R. A., R. L. Davidson, and R. A. Heelis (2012), Ion drift meter calibration and photoemission correction for the C/NOFS satellite, *J. Geophys. Res.*, *117*, A08323, doi:10.1029/2012JA017636.

Subbarao, K. S. V., and B. V. Krishna Murthy (1994), Post-sunset *F* region vertical velocity variations at magnetic equator, *J. Atoms. Terr. Phys.*, *56*, 59–65, doi:10.1016/0021-9169(94)90176-7.

Sultan, P. J. (1996), Linear theory and modeling of the Rayleigh-Taylor instability leading to the occurrence of the equatorial spread *F*, *J. Geophys. Res.*, *101*, 26,875–26,891, doi:10.1029/96JA00682.

Tsunoda, R. T. (1985), Control of the seasonal and longitudinal occurrence of equatorial scintillations by the longitudinal gradient in integrated *E* region Pedersen conductivity, *J. Geophys. Res.*, *90*, 447–456, doi:10.1029/JA090iA01p00447.

Tsunoda, R. T., M. Yamamoto, T. Tsugawa, T. L. Hoang, S. Tulasi Ram, S. V. Thampi, H. D. Chau, and T. Nagatsuma (2011), On seeding, large-scale wave structure, equatorial spread *F*, and scintillations over Vietnam, *Geophys. Res. Lett.*, *38*, L20102, doi:10.1029/2011GL049173.

Tulasi Ram, S., P. V. S. Rama Rao, K. Niranjan, D. S. V. V. D. Prasad, R. Sridharan, C. V. Devasia, and S. Ravindhran (2006), The role of post sunset vertical drifts at the equator in predicting the onset of VHF scintillations during high and low sunspot activity years, *Ann. Geophys.*, *24*, 1609–1616, doi:10.5194/angeo-24-1609-2006.

Tulasi Ram, S., M. Yamamoto, R. T. Tsunoda, S. V. Thampi, and S. Gurubaran (2012), On the application of differential phase measurements to study the zonal large scale wave structure (LSWS) in the ionospheric electron content, Radio Science, *Rad. Sci.*, *47*, RS2001, doi:10.1029/2011RS004870.

Tulasi Ram, S., M. Yamamoto, R. T. Tsunoda, H. D. Chau, T. L. Hoang, B. Damtie, M. Wassaie, C. Y. Yatini, T. Manik, and T. Tsugawa (2014), Characteristics of large scale wave structure observed from African and Southeast Asian longitudinal sectors, *J. Geophys. Res. Space Physics*, *119*, 2288–2297, doi:10.1002/2013JA019712.

Yizengaw, E., J. Retterer, E. E. Pacheco, P. Roddy, K. Groves, R. Caton, and P. Baki (2013), Postmidnight bubbles and scintillations in the quiet-time June solstice, *Geophys. Res. Lett.*, *40*, 5592–5597, doi:10.1002/2013GL058307.

Yokoyama, T., S. Fukao, and M. Yamamoto (2004), Relationship of the onset of equatorial *F* region irregularities with the sunset terminator observed with the Equatorial Atmosphere Radar, *Geophys. Res. Lett.*, *31*, L24804, doi:10.1029/2004GL021529.

Yokoyama, T., M. Yamamoto, Y. Otsuka, M. Nishioka, T. Tsugawa, S. Watanabe, and R. F. Pfaff (2011), On postmidnight low-latitude ionospheric irregularities during solar minimum: 1. Equatorial Atmosphere Radar and GPS-TEC observations in Indonesia, *J. Geophys. Res.*, *116*, A11325, doi:10.1029/2011JA016797.